Technical University of Denmark

DTU

The flow upstream of a row of aligned wind turbine rotors and its effect on power production

Meyer Forsting, Alexander Raul; Troldborg, Niels; Gaunaa, Mac

DTU Library
Technical Information Center of Denmark

The blockage induced rise in power production for laterally aligned wind turbines

A. R. Meyer Forsting, N. Troldborg, M. Gaunaa

[1] DTU Wind Energy, Department of Wind Energy, Technical University of Denmark, Risø Campus, DK-4000 Roskilde, Denmark

E-mail: `alrf@dtu.dk`

Abstract. The blockage developing in front of a laterally aligned row of wind turbines and its impact on power production over a single turbine was analysed using two different numerical methods. The inflow direction was varied from orthogonal to the row until $45°$, with the turbines turning into the wind, thereby resembling a wind turbine testing site or row in a wind park. The numerical methods included computational fluid dynamics (CFD) with an actuator disc representation of the rotor and a simple vortex method. The forces on the actuator disc were either derived from airfoil data of a modern wind turbine or set as constant. For all methods significant changes were found in the developing flow-field with corresponding effects on the individual power output of the wind turbines. These became more pronounced with increasing inflow angle and predicted a rise in power of up to 2% for the downstream and -1% for the upstream turbines. The vortex method agreed with the CFD method on the overall trend, but its magnitude was lower.

1. Introduction

Whereas the layout of onshore wind farms is mostly governed by the site-specific topology and planning permits, offshore developments offer more freedom regarding the placement of individual turbines. To a certain extent this allows for the optimisation of the placement of turbines, such that the losses in power production incurred by wakes can be minimised. If wake effects are ignored the potential power deficit could reach up to 35 % relative to isolated turbines [1]. This marked impact of wakes explains the limited attention that has been paid to blockage effects on power production in wind farms. The velocity deficit induced upstream by the turbine is more local and less pronounced, meaning it is commonly assumed to be negligible in the wider context [2].

For tidal wave turbines, on the other hand, it has been shown experimentally [3] and numerically [4, 5] that inter turbine blockage significantly increases power production. Nevertheless for wind turbines these findings are not replicable as they operate in a free domain, unrestricted by water depth. The upstream blockage in a wind engineering context has recently been studied in numerous low Reynolds number experiments. For a single turbine Medici *et al.*

detected a velocity deficit up to three diameters (D) upstream using hot-wire anemometry and particle image velocimetry [6]. McTavish *et al.* made use of similar techniques to quantify the blockage for three laterally aligned, small scale wind turbines, which were placed perpendicular to the inflow [7]. Reducing the lateral spacing from $2D$ to $1.5D$, they found an increase in power across all three turbines with the central turbine gaining the most. Summing the increase in power for all three turbines over an isolated turbine, they found a 6% and 17% power surge, respectively. The influence of a wind tunnel blockage of 5% on the results was not determined, nevertheless a vortex particle simulation seemed to confirm the results. That these variations in power are not limited to simulations and wind tunnel experiments has been shown by Mitraszewski *et al.* [8] who analysed the power production along the outer rows of turbines in the Horns Rev 1 wind farm. Here the power relative to the mean of the whole wind park varied up to ±5%.

While over an entire wind farm these changes might be minuscule, they might have significant implications for turbine power curve verification. Test sites such as those in Høvsøre and Østerild in Denmark align turbines on an axis perpendicular to the prevailing wind direction and by the widely used IEC standards, allow measurements up to 45° to the alignment axis. It is at least questionable if at these large inflow angles the power variations remain negligible. From the current literature it is not possible to determine whether blockage impacts the current power curve evaluations, as all inflows were perpendicular to the line of turbines. Furthermore most findings are based on low Reynolds number experiments and used extremely small lateral spacings relative to those in a real setting.

In this paper a set-up loosely related to the DTU test site at Høvsøre is adopted, where the angle between the inflow and turbine alignment axis is varied. A CFD model in combination with an actuator disc (AD) is employed to evaluate the power changes over five 5-MW reference turbines. The turbines have zero yaw error and no boundaries are taken into account. The more realistic reference turbines are replaced by constantly loaded discs to exclude turbine design specific effects and allow a comparison with simpler vortex methods. The results are discussed with respect to the blockage induced flow-field and the wind farm power data.

1.1. Problem definition

The DTU testing site Høvsøre represents an arrangement for which lateral blockage might be relevant. A loosely related setup consisting of five aligned turbines with a $3D$ lateral spacing was therefore adopted (see Figure 1). Taking current measuring procedures as a reference, the angle between the line of wind turbines and the main wind direction (θ) was varied from 0° to 45° in 15° steps. Note that θ will sometimes be referred to as 'yaw' in the following passages. The inflow was set to be uniform at 8 m/s. Furthermore the solution was assumed to be time invariant.
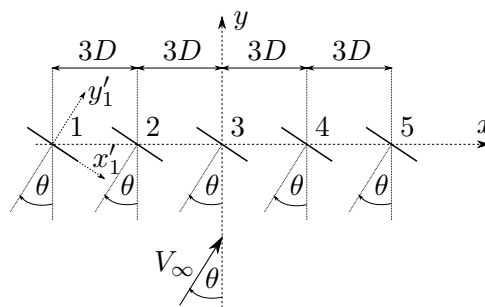

Figure 1. Schematic of the wind turbines' arrangement and reaction to changing inflow directions.

2. Computational method

2.1. CFD

2.1.1. Flow solver The flow field is solved via the in-house developed finite volume code EllipSys3D. It solves the incompressible Reynolds Averaged Navier-Stokes (RANS) equations over a discretized block-structured domain [9–11]. The SIMPLE algorithm [12] computes the pressure-linked terms of the Navier-Stokes equations, whereas the QUICK scheme [13] determines the convective terms. A modified Rhie-Chow algorithm avoids the tendency of decoupling velocity and pressure from implementing discrete body forces inside the domain [14–16]. The turbulence was incorporated via the Menter $k-\omega$ shear-stress transport model [17].

2.1.2. Turbine model The turbine rotor was represented by a permeable actuator disc. The discrete body forces acting over the disc are either determined iteratively from the local blade velocities and airfoil data or are predefined. In the former type of force allocation the airfoil data and geometry of the NREL 5-MW [18] with a 126 m diameter rotor was used. At the set wind speed of 8 m/s, the rotor performs 9.21 rotations per minute (RPM).

To arrive at a more general description of the laterally induced blockage the NREL 5-MW turbines were subsequently replaced by constantly loaded discs. The global thrust coefficient C_T of a single NREL turbine at $V_\infty = 8$ m/s equalled 0.798. The normal force thus acting over a sectional area ΔA of the actuator disc is:

$$F_N = \frac{1}{2}\rho_\infty V_\infty^2 C_T \Delta A \qquad (1)$$

, with $\rho_\infty = 1.225$ kg/m^3 and R equalling the rotor radius. Note that approximating the influence of a rotor with only normal forces correspond to the ideal case where the tip speed ratio tends to infinity.
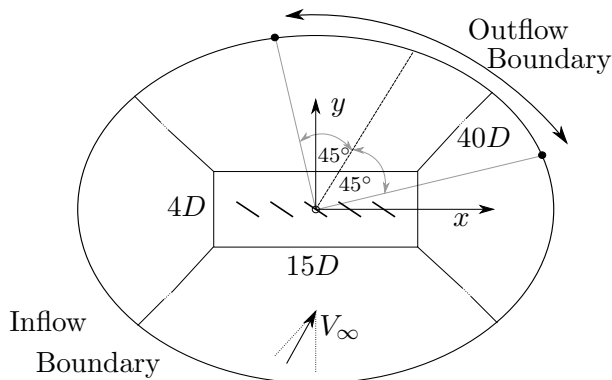
Figure 2. Top view of the numerical domain. All dimensions are scaled by the turbine diameter D. Note that the boundaries are a function of the inflow angle.
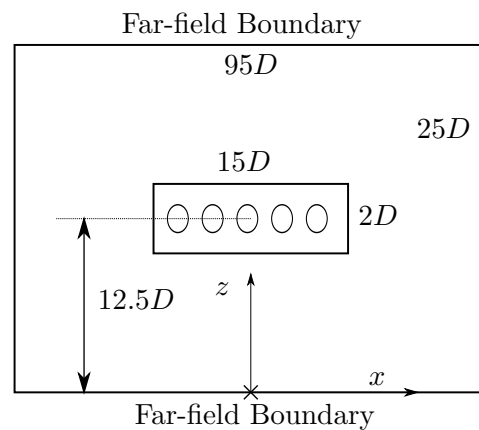
Figure 3. Frontal view of the numerical domain.

2.1.3. Numerical domain The numerical domain was discretized by a structured O-type meshing methodology, containing a centrally located equispaced box mesh. The latter encompassed the row of turbines. Farfield boundary conditions were applied to both, top and bottom of the domain, i.e. the ground and the atmospheric boundary layer were not modelled. The in- and outflow boundaries were applied dynamically to the sides of the O-mesh by the pre-processor, depending on the inflow angle. More specifically the outflow sector encompassed

$\pm$ 45° centred around the inflow direction. A schematic layout of the domain and its coordinate system is shown in Figures 2 and 3. All dimensions were scaled by D. The spacing inside the central box was $D/32$ in all directions. From there the mesh grew hyperbolically outwards in the radial and z directions, where the dimension of the first cell matched that of the inner box. The number of grid spaces along the radial and z directions were 32 and 128, respectively. The total number of cells was 2.05×10^6.

It should be noted that the relatively large numerical domain causes the domain blockage to be negligible.

For a full domain and mesh sensitivity analysis refer to the previous work by the authors [19].

2.2. Vortex method

The vortex model used in the present work is based on the method originally proposed by Øye [20] and is described in more detail in Appendix 5. The basis of this model is formed by a turbine with uniform circulation along each blade, where the product of total circulation and rotational speed remains constant, as the former tends to zero and the latter to infinity. This corresponds to simulating a constant loaded disc where the thrust coefficient, c.f. equation (Appendix A.3) is:

$$C_T = \frac{\Gamma \Omega}{\pi V_\infty^2} \qquad (2)$$

where Γ is the summed circulation of all blades, Ω the rotational speed and V_∞ is the free-stream velocity.

The wake of each turbine is modelled using discrete vortex rings in the near wake and a semi-infinite vortex cylinder in the far-wake. In the first part of the near wake the rings are allowed to expand while in the last part the ring radius is kept constant. In this paper the initial 30 rotor radii of the wake was simulated with vortex rings with a streamwise spacing of 0.1 rotor radii. In the first 29 rotor radii the rings can expand freely while their radius is fixed in the last part.

3. Results

3.1. The flow-field
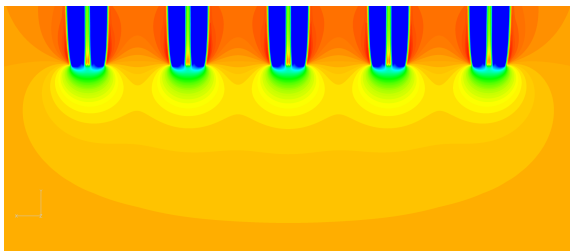
Figure 4. Normalised axial velocity contours (v_a/V_∞) in the xy-plane at a yaw angle (θ) of 0° and with the NREL 5-MW turbine model.
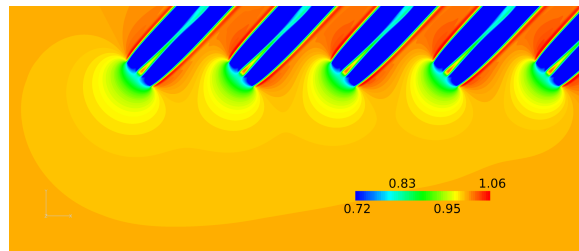
Figure 5. Normalised axial velocity contours (v_a/V_∞) in the xy-plane at a yaw angle (θ) of 45° and with the NREL 5-MW turbine model.

In Figures 4 and 5 axial velocity contours for inflow angles of 0° and 45° are shown, respectively. Both are xy-planes extracted at hub height and simulated with CFD using the NREL 5-MW turbine model. The contours reveal the emergence of a 'global' induction zone along the entire turbine row, as they start to act as one single flow obstruction. Unsurprisingly

this global effect is symmetric for a perpendicular inflow, hence its extent is largest at the central turbine. Moving the inflow brakes the symmetry and the upstream turbine (1) starts to experience the strongest velocity deficit. Along the turbines the flow velocity starts to recover. This effect is amplified in-line with increasing the inflow angle.

In-between the individual induction zones the flow is accelerated. This channelling aggravates with increasing inflow angle, as the cross-sectional area normal to the flow direction is further constrained by the wake of the neighbouring turbine. The direct consequence is the development of non-symmetric local induction zones, since the flow accelerates towards the wake.
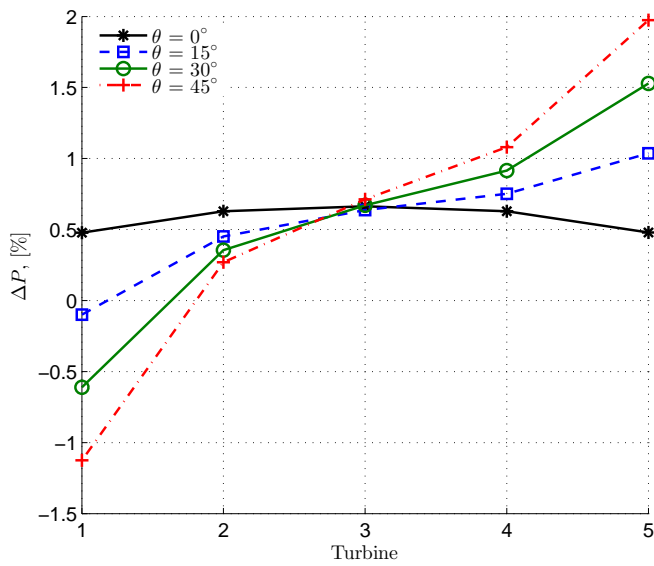
3.2. Power evolution

Figure 6. Percentage change in the power coefficient for different yaw angles.
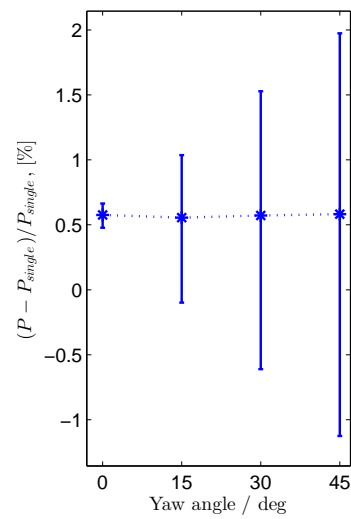
Figure 7. Summary of mean, minimum and maximum values of the results in Figure 6 as a function of yaw angle.

3.2.1. NREL 5-MW In Figure 6 the evolution of global power coefficients along the row of turbine is shown for all four inflow angles. The change in power for each turbine is calculated with respect to an isolated turbine at the same location and orientation i.e.:

$$\Delta P|_{i,j} = \frac{P|_{i,j} - P_{single}|_{i,j}}{P_{single}|_{i,j}} \times 100 \tag{3}$$

,with $i = \{1,\ldots,5\}$ and $j = \{0°, 15°, \ldots, 45°\}$. The mean and extrema are plotted as a function of θ in Figure 7. Note that turbine 1 is upstream i.e. on the far left in Figure 5. A flow perpendicular to the row ($\theta = 0$) is shown to increase the power output universally above 0.5% compared to an isolated turbine. This global rise and the gain towards the central turbine is in line with the work of McTavish *et al.* [7]. Using half the lateral spacing compared to this study ($1.5D$) he found larger gains in power of up to 8 % for the central turbine. Even when matching all parameters of his numerical simulations, in particular the turbine thrust coefficient, C_T, and lateral spacing, only an increase of 3 % is registered. This discrepancy is most likely related to the markedly different rotor designs and numerical methods employed. Nevertheless the trend is clear.

The change in power across the turbines is altered significantly once the inflow is yawed, except for the central turbine, where ΔC_P is about constant for any θ. All curves start to demonstrate an anti-symmetry about the central turbine for $\theta \neq 0°$. The losses upstream translate to additional gains downstream, which is underlined by quasi constant mean power rise of 0.57% across the turbines (see Figure 7). The amplitude increases rapidly with inflow angle and reaches 3.1% for $\theta = 45°$.

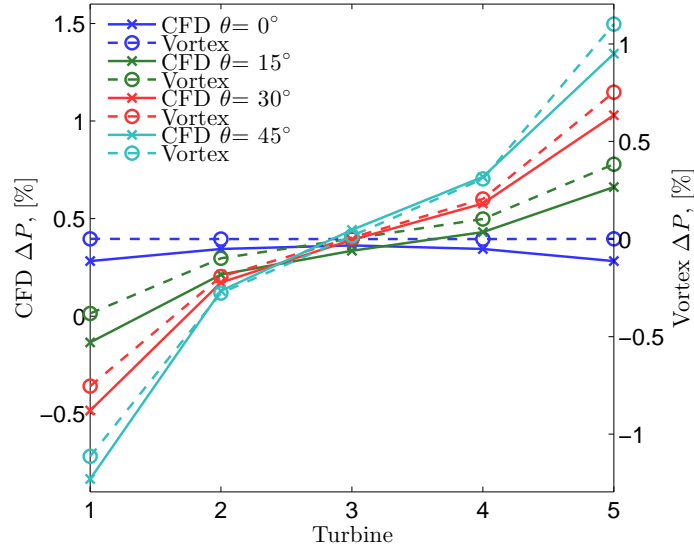**Figure 8.** Comparison of the percentage changes in the power coefficient for different inflow angles θ between CFD-AD simulations and the vortex method. They are presented with respect to two independent y-axes, but equal scaling. The axes are shifted by 0.4% to each other.

3.2.2. Comparison CFD - vortex method   Replacing the NREL turbine with a constantly loaded disc does not alter the overall behaviour of the solution, as shown in Figure 8. The magnitude of the percentage changes in the C_P has dropped relative to the NREL simulations, but still shows a net rise in the C_P for the constantly loaded discs. In Figure 8 the y-axis of the vortex solutions (on the right) is shifted upwards by 0.4%, as it consistently under-predicts the power relative to CFD. Nevertheless the scale is left unchanged, which essentially demonstrates that both methods agree on the changes in power upstream and downstream relative to the central turbine.

4. Discussion
The overall rise in C_P and the significant changes in the individual turbine power production can be related to the emerging flow-field. As mentioned in Section 3.1 the flow is accelerated in-between turbines and along the row of turbines in case of yawed inflows. Almost equal to the acceleration along the turbines is the stronger deceleration in front of the upstream turbines. It is this balance that ensures that power production for the entire row is essentially unchanged by alterations in the inflow angle. Furthermore it underlines that global changes in the induction zone are determining the individual power output, instead of local ones. Decreasing the distance between turbine and neighbouring wake with increasing inflow angle, does not seem to accelerate

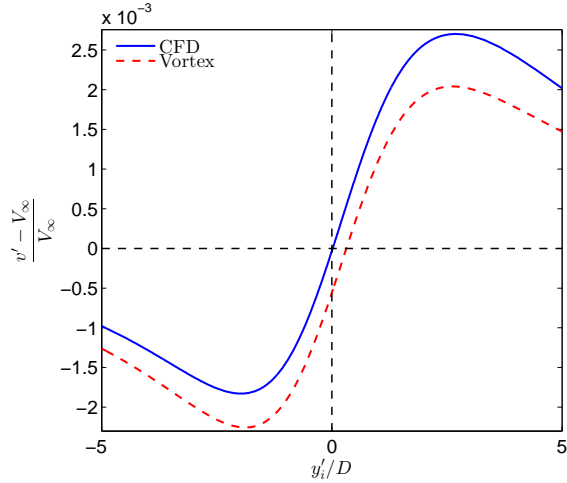the flow sufficiently to noticeably impact the power evolution along the row.

Figure 9. Streamwise velocity induced along y at $x/D = 3$ predicted by CFD and the vortex method by a single turbine located at $x/D = 0$.

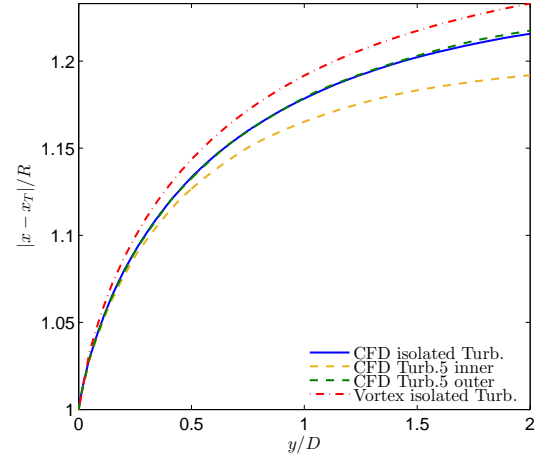**Figure 10.** Radial wake expansion for an isolated turbine predicted by CFD simulations and vortex method at $\theta = 0°$, as well as the inner and outer wake expansion in x for turbine 5. All turbines had uniform loading.

The ensuing flow-field itself is directly related to the wake induced velocities. Figure 9 shows the velocity induced by an isolated, constantly loaded turbine located at the centre of the domain ($x/D = 0$) on the line $x/D = 3$ (i.e. a line that would coincide with the centreline of a neighbouring turbine). For both CFD and the vortex method a positive velocity is induced downstream of $y/D > 0$ and negative upstream. In the CFD simulation the velocity induced downstream is larger than the one upstream. The opposite is the case for the vortex method, though similar to the comparison in Section 3.2.2 it is mainly an offset differentiating both methods. In general the positive induced velocities found for $y/D > 0$ signify that if there was a turbine placed at $x/D = 3$, its wake would be advected more quickly under the neighbouring turbine's influence. This would in turn reduce the negative velocity induced by the wake in front of the turbine and diminish the local blockage. In the case of $\theta = 0°$ all turbine wakes are influencing each other in a similar fashion, with the only difference being that the inner turbines are experiencing the combined induced velocities of their neighbours. As each turbine's wake induces a positive velocity behind its rotational plane, yawing the turbines will thus lead to the summation of induced positive velocities. Meaning that the last turbine experiences the added induced velocities of four turbines. Reciprocally, all negative velocities are adding up from the downstream towards the upstream turbines, leading to a stronger induction zone in front of the first turbines. Following this argument including the ground would enlarge the induced velocities considering the image vortices of the turbines.

The difference in induced velocities shown in Figure 9 is directly related to the wake expansion predicted by each method. As shown in Figure 10, the wake is expanding more rapidly using the vortex method. Especially close to the rotor do the two methods disagree. The simple vortex method captures the overall trend predicted by the CFD simulations for yawed inflows, but does not show an overall increase in the power across the row of turbines. This is most likely due to some non-linear effects influencing the interplay of wakes that are not captured by the vortex method as its wakes are inherently axisymmetric. This impacts the induced velocities and in

turn wake expansion. In Figure 10 the evolution of the wake radius of the outermost turbine (5) from a CFD simulation at $\theta = 0°$ is shown. The inner side of the wake is expanding less than the outer part, due to the channelling of the flow in-between turbines. This kind of wake straightening towards the inner turbines was also observed numerically and experimentally by McTavish *et al.* [7]. Additionally to the wake straightening, their free expansion in the vertical plane results in slightly elliptical wakes in the CFD computations opposing the assumption of axisymmetry. The wake radii determined for the CFD calculations are estimated from mass conservation, though this might not be a very accurate representation, it demonstrates that the wake radii differ between methods, which might explain some of the discrepancies between CFD and vortex code.

Yet another explanation might be related to the numerical implementation of the actuator disc. Whereas the forces in the vortex method act over an infinitesimally thin disc, they act over several grid cells in the computational mesh of the CFD simulations, potentially influencing the rate of wake expansion [21].

5. Conclusion

The lateral blockage induced by a row of five wind turbines and its impact on power production was determined from numerical simulations with CFD and a vortex-based method.

The interaction of the wind turbine wakes leads to the development of a large decelerating region in front of the entire row of rotors. Locally each turbine induces the strongest blockage, causing the expanding flow to accelerate in-between them. This was especially pronounced once the inflow angle increased, resulting in asymmetrically shaped local induction zones. However, it is the combined 'global' blockage from all turbines that determines the changes in power production.

The negative velocities induced by the wakes in front of their respective rotor planes combine and lead to a growing deceleration in front of the upstream turbines, leading to a power loss of up to 1% for the most upstream NREL turbine at an inflow angle of 45°. The positive velocities induced behind the rotor planes on the other hand induce an acceleration towards the downstream turbines, that in the most extreme case could yield a 2% increase in power output.

To test the reproducibility of these results the set-up was recreated using a vortex method and the same CFD methodology only replacing the NREL turbine with a constantly loaded actuator disc. The loading matched that of the NREL turbine. Though the magnitude of the results was lower for both methods, the overall trends described above remained observable. The discrepancy between vortex and CFD method were attributed to non-linear effects on individual wake expansion. Whereas it was fixed for all turbines in the vortex computations, the CFD results showed variations depending on turbine position.

For wind turbine testing sites it is of utmost importance to accurately measure the power performance of individual turbines. Therefore even the limited variations in the power output found in this investigation might proof to be significant. It is to be seen whether the findings persist once a more realistic flow, including an atmospheric boundary layer, is employed. However, for now the power evolution found in the Nysted wind farm is promising.

References

[1] Barthelmie R, Frandsen S, Hansen K, Schepers J, Rados K, Schlez W, Neubert A, Jensen L and Neckelmann S 2009 Modelling the impact of wakes on power output at nysted and horns rev *Proc. of the European Wind Energy Conference*

[2] *IEC 61400-12-1:2005, Power performance measurements of electricity producing wind turbines.*

[3] Bahaj A, Molland A, Chaplin J and Batten W 2007 *Renewable Energy*

[4] Turnock S R, Phillips A B, Bank J and Nicholls-Lee R 2011 *Ocean Engineering*

[5] Nishino T, Richard and Wilden H 2012 *J. Fluid Mech.*

[6] Medici D, Ivanell S, Dahlberg J A and Alfredsson P 2011 *Wind Energy*

[7] McTavish S, Rodrigue S, Feszty D and Nitzsche F 2014 *Wind Energy*

[8] Mitraszewski K, Hansen K, Nygaard N and Réthoré P E 2012 Wall effects in offshore wind farms *Torque 2012*

[9] Sørensen N 1995 *General purpose flow solver applied to flow over hills* Ph.D. thesis RisøNational Laboratory

[10] Michelsen J 1994 Basis3d - a platform for development of multiblock pde solvers Tech. rep. Dept. of Fluid Mechanics, Technical University of Denmark, DTU

[11] Michelsen J 1994 Block structured multigrid solution of 2d and 3d elliptic pdes Tech. rep. Dept. of Fluid Mechanics, Technical University of Denmark, DTU

[12] Patanker S and Spalding D 1972 *International Journal of Heat and Mass Transfer*

[13] Leonard B 1979 *Computer Methods in Applied Mechanics and Engineering*

[14] Réthoré P E and Sørensen N 2012 *Wind Energy*

[15] Réthoré P E and Sørensen N 2013 *Wind Energy*

[16] Troldborg N, Sørensen N, Réthoré P E and van der Laan M 2015 *Computers & Fluids*

[17] Menter F R 1993 *AIAA Journal*

[18] Jonkerman J, Butterfield S, Musial W and Scott G 2009 Definition of a 5-mw reference wind turbine for offshore system development Tech. rep. NREL

[19] Meyer Forsting A and Troldborg N 2015 *Journal of Physics: Conference Series (Online)* **625** ISSN 1742-6596

[20] Øye S 1990 A simple vortex method *Proc. of the third IEA Symposium on the Aerodynamics of WindTurbines* (Institute of Physics Publishing)

[21] Troldborg N, Zahle F, Réthoré P E and Sørensen N 2013 *Wind Energy* 10.1002/we.1757

[22] Branlard E and Gaunaa M 2014 *Journal of Wind Energy*

Appendix A. A simple vortex model including wake expansion

The model used in the present work is a modified version of the model proposed by Øye [20]. In the following the basics of the model will be briefly described.

Appendix A.1. Rotor circulation and loads

The model considers an idealized wind turbine where each blade is represented by a line with a constant circulation of Γ_b. The flow field is assumed incompressible, irrotational and inviscid so the forces per unit span of the the rotating lines is given by the the Kutta-Joukowski relation:

$$\boldsymbol{f}_b = \rho \boldsymbol{V}_{\text{rel}} \times \boldsymbol{\Gamma}_b \qquad \text{(Appendix A.1)}$$

where $\boldsymbol{V}_{\text{rel}}$ is the local velocity relative to the blade and ρ denotes density. The local force per unit area in the radial, tangential (driving force) and axial direction, respectively then becomes

$$\boldsymbol{F} = \left[\begin{array}{c} F_r \\ F_\theta \\ F_z \end{array} \right] = \frac{N_b \boldsymbol{f}_b dr}{2\pi r dr} \frac{\rho \Gamma \Omega}{2\pi} \left[\begin{array}{c} 0 \\ (V_\infty + W_z)/(\Omega r) \\ 1 - W_\theta/(\Omega r) \end{array} \right] \qquad \text{(Appendix A.2)}$$

Here, $\Gamma = n_b \Gamma_b$ is the total circulation of all n_b blades, Ω is the rotor rotational velocity, r is the radius where the forces are evaluated and V_∞ is the free stream velocity, which is assumed to be parallel to the rotor axis. W_z and W_θ are the induced velocities in the axial and tangential directions at the rotor plane, respectively.

In the following we now assume that the rotational speed of the rotor tends to infinity and the

total circulation to zero, such that their product becomes a finite value. In that case only the axial force component remains and equation (Appendix A.2) simplifies to:

$$F_z = \frac{\rho \Gamma \Omega}{2\pi}$$ (Appendix A.3)

Note that in order to retain a finite value of the rotor force, the product $\Gamma\Omega$ needs to be finite, i.e. $\Gamma \to 0$.

Appendix A.2. Modelling the wake

The present model is a so-called vortex model. Thus, the velocity is determined from the vorticity in the wake using the Biot-Savart law. Because the vortex strength is constant along each blade, vorticity will only be trailed from the roots and tips. Since the incoming wind is further assumed to be uniform and aligned with the rotor axis, the root vortices merge to a single axial vortex of strength Γ, while the tip vortices forms a circular tube of vorticity with increasing radius as the wake expands. However, a consequence of the infinitely high rotational speed is that the strength of the root vortex tends to zero (as shown above), i.e. there is no wake rotation and that the density of the tip vorticity sheet only has a tangential component, $\gamma_t = d\Gamma/dz$. The value of γ_t is most easily obtained by acknowledging that the vortex strength between two windings of the tip vortex produced by one of the blades is Γ, i.e.:

$$\gamma_t(z) = \frac{\Gamma \Omega}{2\pi V_a(z)}$$ (Appendix A.4)

where V_a is the axial velocity at which the tip vortices are transported.

As in the original model by Øye [20] the near wake, where the wake is expanding, is modelled
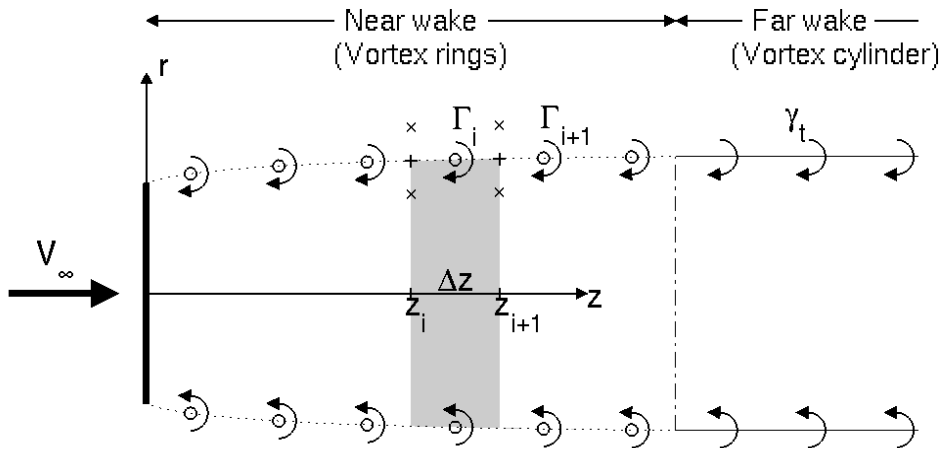

Figure A1. *Model of near and far wake with discrete vortex rings and a vortex cylinder, respectively.*

using discrete vortex rings, while the far wake, is modelled using a half-infinite circular vortex

cylinder with constant γ_t and radius, see Figure A1. When the induction from each vortex ring as well as from the cylinder is known, then the total induced velocity W everywhere is determined by simply adding all contributions together.

Appendix A.2.1. Modelling the near wake The near wake is modelled using discrete vortex rings, where each ring are allowed to expand freely. The velocity induced by a vortex ring in a point P is [20]:

$$w_z(r, z) = \frac{\Gamma_i}{2\pi\sqrt{(r + R)^2 + z^2}} \left(\frac{R^2 - r^2 - z^2}{(r - R)^2 + z^2} \cdot E(k^2(z)) + K(k^2(z)) \right) \qquad \text{(Appendix A.5)}$$

$$w_r(r, z) = \frac{\Gamma_i}{2\pi\sqrt{(r + R)^2 + z^2}} \frac{z}{r} \left(\frac{r^2 + R^2 + z^2}{(r - R)^2 + z^2} E(k^2(z)) - K(k^2(z)) \right) \qquad \text{(Appendix A.6)}$$

with

$$k^2(z) = \frac{4Rr}{(r + R)^2 + z^2}$$

where r and z are the radial and axial coordinates, respectively of P relative to the ring center, Γ_i is the strength of the ring and R is the radius of the ring, which is equal to the local wake radius. Finally, E and K are the complete elliptic integral of first and second kind, respectively. As shown in Figure A1, each ring represents a segment of the wake of length Δz and because the ring is positioned in the center of the segment its strength is

$$\Gamma_i = \frac{1}{2} \left(\gamma_t(z_i) + \gamma_t(z_{i+1}) \right) \Delta z \qquad \text{(Appendix A.7)}$$

In order to get the vortex density we need to determine V_a. As suggested by Øye [20] we assume that V_a is the average of the velocity on each side of the wake surface. Thus for a downstream position z_i, we get:

$$V_a(z_i) = V_\infty + \frac{1}{2} \left(W_z(R_w(z_i) + \Delta r, z_i)) + W_z(R_w(z_i) - \Delta r, z_i)) \right) \qquad \text{(Appendix A.8)}$$

where Δr is a small distance selected by the modeller (indicated with a "×" in Figure A1) and W_z is the total induced velocity from all vortex rings as well as from the vortex cylinder, representing the far wake.

The local wake radius is computed from the continuity equation and the fact that the wake surface is a streamtube, which implies that the flow through the rotor disc is the same as through each wake cross-section. Thus, the local wake radius at $z = z_i$ is

$$R_w(z_i) = R\sqrt{\frac{V_\infty + \bar{W}_z(0)}{V_\infty + \bar{W}_z(z_i)}} \qquad \text{(Appendix A.9)}$$

where R is the radius of the rotor and $\bar{W}_z$ is the average induced velocity over the wake cross-section at $z = z_i$ downstream of the rotor, i.e.

$$\bar{W}_z(z_i) = \frac{1}{\pi R_w(z_i)^2} \int_0^{2\pi} \int_0^{R_w(z_i)} W_z(r, \theta, z_i) r \, dr \, d\theta \qquad \text{(Appendix A.10)}$$

Here, the dependency of W_z on azimuth position θ is explicitly shown because the present model is also used for computing multiple turbines next to each other where the velocity in the wake is not axisymmetric. Since the induced velocity depends on γ_t, which in turn depends on V_a and the local wake radius the equations (Appendix A.7)-(Appendix A.10) need to be solved iteratively to determine the the strength and radius of the vortex rings.

Appendix A.2.2. Modelling the far wake Going downstream from the rotor the wake gradually stops expanding and therefore the far wake is modelled with a half infinite cylinder of constant γ_t and radius, both equal to the values of the last section in the near wake. Øye suggested to approximate the contribution from the cylinder to the total induction as the induction along its centreline. Here, we instead use the full velocity field induced by the cylinder, which in a point P is [22]:

$$w_r(r, z) = -\frac{\gamma_t}{2\pi} \sqrt{\frac{R}{r}} \left[\frac{2 - k^2(z)}{k(z)} K\left(k^2(z)\right) - \frac{2}{k(z)} E\left(k^2(z)\right) \right]$$

(Appendix A.11)

$$w_z(r, z) = \frac{\gamma_t}{2} \left[\frac{R - r + |R - r|}{2|R - r|} + \frac{zk(z)}{2\pi\sqrt{rR}} \left(K\left(k^2(z)\right) + \frac{R - r}{R + r}\Pi\left(k^2(0), k^2(z)\right) \right) \right]$$

(Appendix A.12)

where r and z is the radial and axial position of P relative to the center of the cylinder front, R is the radius of the cylinder which is equal to the far wake radius and Π is the complete elliptic integral of the third kind. The solution for the velocity near at the axis of the cylinder is:

$$w_r(0, z) = 0; \qquad w_z(0, z) = \frac{\gamma_t}{2} \left[1 + \frac{z}{\sqrt{R^2 + z^2}} \right]$$

(Appendix A.13)

For $r = R$ the axial induction is

$$w_z(R, z) = \frac{\gamma_t}{4} + \frac{\gamma_t}{2} \frac{zk(z)}{2\pi\sqrt{rR}} K\left(k^2(z)\right)$$

(Appendix A.14)

Appendix A.3. Model set-up
The accuracy of the above model depends on the chosen streamwise extent of the near wake, the spacing between the vortex rings, Δz, the distance Δr used to compute the transport velocity, Eq. (Appendix A.8), and the method used for computing $\bar{W}_z(z)$.

In this paper we use $\Delta z = \Delta r = R/10$ as suggested by Øye [20]. Here, the near wake length is here set to $30R$, which is significantly longer than the $5R$ used by Øye. The extended near wake length is necessary to accurately capture the mutual effect the near wake of each turbine has on each other. In the simulation of a single turbine Øye [20] assumes that the velocity at 70% radius is representative of the average velocity at each cross-section, i.e. $\bar{W}_z(r, z) = W_z(0.7R_w, z)$. Here we instead approximate $\bar{W}_z(z)$ by computing the integrals in equation (Appendix A.10) using the trapezoid rule with a discretization of $dr = R_w/10$ and $d\theta = \pi/2$. Thus the average velocity over the entire cross-section is estimated as the average of the integrated velocity at four azimuthal positions corresponding to the two vertical and horizontal directions. The use of several azimuthal positions is intended to take into account that the flow is not axisymmetric when considering several turbines next to each other.